High-Bandwidth Demodulation in Multifrequency AFM: A Kalman Filtering Approach

Michael G. Ruppert, *Student Member, IEEE*, David M. Harcombe, and S. O. Reza Moheimani, *Fellow, IEEE*

Abstract—Emerging multifrequency atomic force microscopy (MF-AFM) methods rely on coherent demodulation of the cantilever deflection signal at multiple frequencies. These measurements are needed in order to close the z-axis feedback loop and to acquire complementary information on the tip-sample interaction. While the common method is to use a lock-in amplifier capable of recovering low-level signals from noisy backgrounds, its performance is ultimately bounded by the bandwidth of the low-pass filters. In light of the demand for constantly increasing imaging speeds while providing multifrequency flexibility, we propose to estimate the in-phase and quadrature components with a linear time-varying Kalman filter. The chosen representation allows for an efficient high-bandwidth implementation on a Field Programmable Gate Array (FPGA). Tracking bandwidth and noise performance are verified experimentally and trimodal AFM results on a two-component polymer sample highlight the applicability of the proposed method for MF-AFM.

Index Terms—Multifrequency Atomic Force Microscopy, State Estimation, Kalman Filter, High-speed, FPGA Implementation

I. INTRODUCTION

THE invention of atomic force microscopy (AFM) [1], made it possible to capture a sample's topographical information with nanometer resolution by coupling the tip of a cantilever to the surface of the specimen [2]. Due to the nonlinear tip-sample forces acting on the cantilever, a feedback loop has to be employed in order to maintain a fixed setpoint with respect to the sample. In amplitude modulation (AM)-AFM [3], the feedback parameter is the demodulated amplitude of the deflection signal but other parameters such as the frequency shift in frequency modulation (FM)-AFM [4] can be employed. In these dynamic imaging modes, the cantilever is usually excited close to its fundamental resonance frequency and the feedback loop is closed by commanding the z-axis nanopositioner. A three dimensional topography image of the sample's surface can be obtained by plotting the control signal against the lateral scan trajectories of the nanopositioner. Specifically, when investigating biologically-relevant samples, AM-AFM can provide the required gentle imaging forces [5] but comes with inherent slow imaging speeds which are detrimental to capturing the typically fast associated dynamics [6].

M. G. Ruppert and D. M. Harcombe are with the School of Electrical Engineering and Computer Science, The University of Newcastle, Callaghan, NSW, 2308, Australia (Michael.Ruppert@uon.edu.au, David.Harcombe@uon.edu.au).

S. O. R. Moheimani is with the Department of Mechanical Engineering, The University of Texas at Dallas, Richardson, TX, 75080, USA (Reza.Moheimani@utdallas.edu).

Manuscript submitted December 30, 2015

In order to go beyond the study of topographical information, modern multifrequency (MF)-AFM methods can be employed. These techniques extend the imaging channels to multiple frequencies in order to obtain the nanomechanical composition of a sample [7]. The frequencies are usually associated with either the higher harmonics, generated by the nonlinearity in the tip-sample force, or with the resonance frequencies of the higher order eigenmodes [8]. This extension has led to novel methods such as higher harmonic imaging [9], band-excitation [10], dual-frequency and off-resonance excitation [11] and multimodal AFM [12]–[14]. The latter setup, as depicted in Fig. 1, enables the nanomechanical characterization of soft matter with high spatial resolution [15]–[17] based on the presence of additional distinct frequency components in the deflection signal.

Recently, it was proposed to estimate the tip-sample force directly, potentially enabling high-bandwidth z-axis control [18]. However in conventional AM-AFM, a fundamental component of the feedback loop is the demodulator, whose function is to obtain amplitude and phase of the cantilever deflection signal. If an AFM setup is optimized for speed, every component in the feedback loop, i.e. the cantilever, the x-, y-, z-axis nanopositioner, the z-axis controller and the demodulator have to be optimized for high bandwidth [19]. High-speed estimation methods, such as single wave detectors based on the peak-hold method [20] and real-time integration [21], have been designed particularly for high-bandwidth amplitude estimation. However, they have no robustness against noise and other frequencies present in the deflection signal which makes them inherently incompatible with modern MF-AFM methods. In contrast, narrowband demodulation performed by a lock-in amplifier (LIA), and its improved version using phase cancellation [22], is more suitable at rejecting unwanted frequency components but at the expense of the measurement bandwidth. The response time is dictated by the post-mixing low-pass filter (LPF), which has to be employed to suppress the frequency component at twice the carrier frequency. As such, it is state of the art to use a number of lock-in amplifiers for MF-AFM experiments; an increasing number of frequencies inevitably renders this approach costly and infeasible.

Motivated by earlier research on tracking power system voltages [23], we previously proposed to employ a Kalman filter with a linear time-varying model of the sinusoid to be estimated. The method was shown to lead to less mixing-induced high-frequency noise and a higher estimation bandwidth than a commercially available lock-in amplifier [24]. In this paper, we extend our previous work to estimating the in-phase and quadrature states of multiple frequencies, related
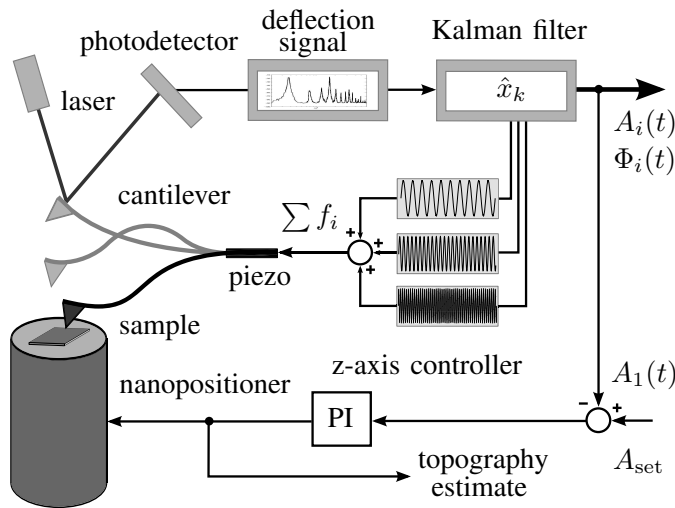
Fig. 1. Schematic of the z-axis feedback loop in trimodal atomic force microscopy using a Kalman filter for demodulation.

to higher harmonics and/or higher eigenmodes in an MF-AFM experiment, simultaneously. The filter is implemented on a Field Programmable Gate Array (FPGA), a tool which is becoming increasingly important in AFM applications [25]. The choice of system representation allows for a high-speed, highly parallelized implementation and avoids the numerical complications that often arise when implementing estimators for highly resonant structures. Numerical results on the tracking bandwidth, robustness to state cross-coupling and the effect of uncertainty in the frequency to be estimated have instigated the excellent suitability of a multifrequency Kalman filter for MF-AFM [26].

In Section II, we outline the time-varying transformation which takes the linear time-invariant model into a form suitable for high-speed digital implementation. We analyze the discrete Kalman filter equations in order to reach a better understanding of its performance and to predict its tracking bandwidth *a priori*. In Section III, we present numerical results on modulating amplitude and phase of a multifrequency signal which forms the basis for a multimodal AFM experiment. In Section IV, we outline the efficient implementation of the Kalman filter on an FPGA and in Section V we present experimental results on demodulating multifrequency signals and compare the estimates with the performance of a state-of-the-art lock-in amplifier. The Kalman filter is compared against the LIA in terms of off-mode rejection and its robustness to white noise is evaluated over a wide tracking bandwidth. In Section VI, we highlight the additional benefit of being able to estimate the static offset in the cantilever deflection signal, simultaneously. Finally, we employ the Kalman filter during trimodal AFM imaging of a soft polymer blend confirming the feasibility of the estimation method for multifrequency Atomic Force Microscopy.

II. SYSTEM MODEL

A. Continuous-time Model

The modal motions $s_i(t)$ of n cantilever eigenmodes can be described by the set of homogeneous differential equations

of simple harmonic oscillators with resonance frequency ω_i given by

$$
\begin{aligned}
\ddot{s}_1(t) + \omega_1^2 s_1(t) &= 0 \\
\ddot{s}_2(t) + \omega_2^2 s_2(t) &= 0 \\
&\vdots \\
\ddot{s}_n(t) + \omega_n^2 s_n(t) &= 0.
\end{aligned}
\tag{1}
$$

Here, each oscillator represents a frequency component whose amplitude and phase are to be estimated. The set of equations can be cast into a state-space model by choosing position $x_{2i-1} = s_i(t)$ and velocity $x_{2i} = \dot{s}_i(t)$ as the state variables and position as the output

$$
\dot{x} = Ax = \begin{bmatrix} A_1 & & 0 \\ & \ddots & \\ 0 & & A_n \end{bmatrix} x
$$

$$
y = Cx = \begin{bmatrix} 1 & 0 & \cdots & 1 & 0 \end{bmatrix} x.
\tag{2}
$$

where each block matrix A_i is represented by

$$
A_i = \begin{bmatrix} 0 & 1 \\ -\omega_i^2 & 0 \end{bmatrix}.
\tag{3}
$$

While the canonical forms (3) are useful in the analysis and understanding of the state equations, the resulting sparse nature of A make them generally ill-conditioned for numerical computations. This can be seen by calculating the condition number κ with respect to a matrix norm of a square matrix [27]. For instance, the 2-norm condition number of the first diagonal block matrix A_1 for a frequency of $\omega_1 = 2\pi 50 \cdot 10^3 \text{rad/s}$ is $\kappa(A_1) \approx 9.9 \cdot 10^{10}$. Further, the condition number will increase for increasing ω and for the overall matrix A, it takes the value of the one relating to the highest ω_i. Therefore, consider the time-variant transformation [24]

$$
T(t) = \begin{bmatrix} T_1(t) & & 0 \\ & \ddots & \\ 0 & & T_n(t) \end{bmatrix}
\tag{4}
$$

with

$$
T_i(t) = \begin{bmatrix} \cos(\omega_i t) & \sin(\omega_i t) \\ -\omega_i \sin(\omega_i t) & \omega_i \cos(\omega_i t) \end{bmatrix}
\tag{5}
$$

such that

$$
x = T(t)\bar{x}.
\tag{6}
$$

Then, a time-variant state-space representation can be obtained by

$$
\begin{aligned}
\dot{\bar{x}} &= \frac{d}{dt}\left(T^{-1}(t)x\right) = \bar{A}\bar{x} \\
\bar{y} &= CT(t)\bar{x} = \bar{C}(t)\bar{x}
\end{aligned}
\tag{7}
$$

which converts (2) into the following form [24]

$$
\dot{\bar{x}} = 0_{2n}\bar{x}
$$

$$
\bar{y} = \begin{bmatrix} \cos(\omega_1 t) & \sin(\omega_1 t) & \cdots & \cos(\omega_n t) & \sin(\omega_n t) \end{bmatrix}\bar{x}
\tag{8}
$$

where 0_{2n} is a $2n$ by $2n$ zero matrix. Here, all the dynamics appear in $\bar{C}(t)$ and the individual sinusoidal components can be recovered via

$$s_i(t) = \bar{x}_{2i-1} \cos(\omega_i t) + \bar{x}_{2i} \sin(\omega_i t)$$
$$= S_i \sin(\omega_i t + \phi_i). \qquad (9)$$

From (9), amplitude and phase of the frequencies of interest can be recovered with

$$S_i = \sqrt{\bar{x}_{2i-1}^2 + \bar{x}_{2i}^2} \qquad (10)$$

$$\phi_i = \arctan\left(\frac{\bar{x}_{2i-1}}{\bar{x}_{2i}}\right). \qquad (11)$$

B. Discrete-time Model

Discretizing (8) with $t = kT_s$, where T_s is the sampling period and adding an additional state to estimate the DC offset [24], yields

$$A_k = e^{\bar{A}kT_s} = I_{2n+1} \qquad (12)$$
$$C_k = [\cos\theta_{1,k} \quad \sin\theta_{1,k} \quad \cdots \quad \cos\theta_{n,k} \quad \sin\theta_{n,k} \quad 1]$$

where $\theta_{i,k} = \omega_i k T_s$ and I_{2n+1} is the identity matrix of dimension $2n+1$. Note, that the condition number $\kappa(A_k) = 1$ is optimal. We consider the states $x_{2i-1,k}$ and $x_{2i,k}$, which dictate amplitude and phase of each sinusoidal component, and $x_{2n+1,k}$, which dictates the DC offset, as random variables. If we assume that the state and output equations are only corrupted by zero-mean Gaussian white noise processes w_k and v_k, the system representation forms the process model for a discrete time-varying (DTV) Kalman filter

$$x_{k+1} = A_k x_k + w_k$$
$$y_k = C_k x_k + v_k$$
$$E[w_k w_k^T] = Q$$
$$E[v_k v_k^T] = R$$
$$E[w_k v_k^T] = 0. \qquad (13)$$

The covariance of the process noise Q indicates the model uncertainty and the covariance of the measurement noise R relates to the quality of the measurements. Note that Q and R have an adverse effect on the Kalman gain K_k and therefore directly influence the amplitude and phase tracking bandwidth. The recursive Kalman filter implementation then consists of iterating between the prediction step using the process model (13) and updating the state estimate and covariance estimate with the Kalman gain [28], [29]. Due to the choice of the system representation, i.e. A_k being the identity matrix, the calculations in the prediction steps are heavily simplified benefiting a high-bandwidth FPGA implementation. Undoubtedly, the computationally most expensive calculation is related to the covariance matrix update, therefore parallelizing and simplifying computations becomes crucial. Here, we chose the Joseph form [28] which maintains the property of symmetry and positive definiteness even if a suboptimal noise covariance matrix Q is assumed in order to maximize the tracking bandwidth of the Kalman filter.

C. Error Dynamics of the DTV Kalman Filter

In order to obtain an estimate of the tracking bandwidth of the Kalman filter, we look at the single frequency case ($n = 1$) and define the Kalman filter priori (prediction) error $\tilde{x}_{k|k-1}$ and the corresponding output error $\tilde{y}_{k|k-1}$

$$\tilde{x}_k = \tilde{x}_{k|k-1} = x_k - \hat{x}_{k|k-1} = A_k \tilde{x}_{k-1|k-1} + w_{k-1} \qquad (14)$$
$$\tilde{y}_k = \tilde{y}_{k|k-1} = y_k - \hat{y}_{k|k-1} = C_k \tilde{x}_{k|k-1} + v_k. \qquad (15)$$

Then we may determine the error model of the Kalman filter to be a linear periodic discrete-time (LPDT) system of the form

$$\tilde{x}_{k+1} = \tilde{A}_k \tilde{x}_k + \tilde{B}_k \tilde{u}_k$$
$$\tilde{y}_k = \tilde{C}_k \tilde{x}_k + \tilde{D}_k \tilde{u}_k \qquad (16)$$

with

$$\tilde{A}_k = A_k(I - K_k C_k)$$
$$\tilde{B}_k = [I \quad -A_k K_k]$$
$$\tilde{C}_k = C_k$$
$$\tilde{D}_k = [0 \quad I]$$
$$\tilde{u}_k = [w_k \quad v_k]^T. \qquad (17)$$

Hence, the estimation error evolves with dynamics dictated by the eigenvalues λ_k of $\tilde{A}_k$. Specifically, we have

$$\tilde{A}_k = \begin{bmatrix} 1 - K_{1,k}\cos\theta_k & -K_{1,k}\sin\theta_k \\ -K_{2,k}\cos\theta_k & 1 - K_{2,k}\sin\theta_k \end{bmatrix} \qquad (18)$$

whose eigenvalues are obtained from

$$\lambda_k^2 + (K_{2,k}\sin\theta_k + K_{1,k}\cos\theta_k - 2)\lambda_k$$
$$+ 1 - K_{2,k}\sin\theta_k - K_{1,k}\cos\theta_k = 0. \qquad (19)$$

Due to the time-varying nature of the Kalman gains K_k and their dependence on the time-varying covariance matrix P_k, finding an analytical expression for the eigenvalues is tedious. However, we notice that the Kalman gains $K_{1/2,k}$ oscillate with equivalent amplitude at the frequency to be estimated, i.e. with ω_1 for the single mode case, are phase shifted by $90°$ and lead the C_k vector entries by φ. Without loss of generality, we can therefore assume that

$$K_{1,k} = K\cos(\theta_k - \varphi) = D\cos\theta_k + E\sin\theta_k$$
$$K_{2,k} = K\sin(\theta_k - \varphi) = D\sin\theta_k - E\cos\theta_k \qquad (20)$$

where $D = K\cos\varphi$ and $E = K\sin\varphi$. Substituting (20) in (19) yields the characteristic equation

$$\lambda_k^2 + (D - 2)\lambda + 1 - D = 0 \qquad (21)$$

whose roots are real and time-invariant and are given by

$$\lambda_{k,1/2} = \begin{cases} 1 \\ 1 - D = 1 - K\cos\varphi. \end{cases} \qquad (22)$$

We notice that one eigenvalue remains fixed at $\lambda_k = 1$ and the other eigenvalue moves closer to the real axis as the Kalman gain increases. This is illustrated in the simulations shown in Fig. 2 for which four different values of the process noise covariance Q are assumed and the respective Kalman filter
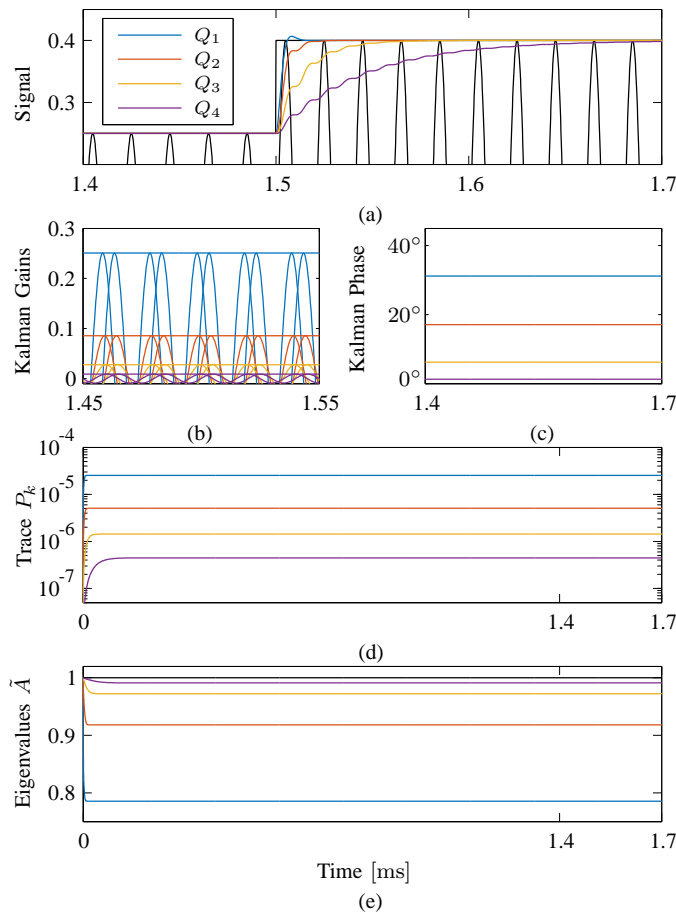
Fig. 2. Simulation of four different Kalman filters assuming decreasing values of Q ($-$, $-$, $-$, $-$) showing (a) single frequency signal ($-$) and its amplitude estimates, (b) Kalman gains, (c) Kalman gain phase, (d) trace of the covariance matrix and (e) eigenvalues of $\tilde{A}_k$ and at $\lambda_k = 1$ ($-$). Simulation Parameters: $f_1 = 50\,\mathrm{kHz}$, $f_s = 5\,\mathrm{MHz}$, $Q_{1/2/3/4} = 10^{-6}/10^{-7}/10^{-8}/10^{-9}$.

aims to track a step change in the amplitude of a single frequency signal $S_1(t)\sin(2\pi f_1 t)$, without additive white noise. Here, the subfigures are color coded and the system shown in blue assumes the largest covariance Q, and the other systems assume a smaller covariance. As can be seen in Fig. 2a, the amplitude tracking bandwidth increases by assuming a larger covariance Q, the only tuning parameter, due to the corresponding increasing Kalman gain amplitudes and phase leads shown in Fig. 2(b) and Fig. 2(c), respectively. This in turn is explained by a higher uncertainty in the model which is expressed by the trace of the covariance matrix P shown in Fig. 2(d), whose minimization is the aim of the Kalman filter. As predicted by (22), the eigenvalues of $\tilde{A}_k$ are real with one eigenvalue constant at one which is plotted in Fig. 2(e). The second eigenvalue was shown to be a function of the Kalman gain amplitude and phase and moves towards zero as Q is increased, resembling a larger tracking bandwidth.

III. SIMULATION

In order to investigate the performance of the multifrequency Kalman filter, we simulate a multi-tonal signal with amplitude and phase modulation. While a change in oscillation

amplitude usually resembles topography features in dynamic AFM, a change in the phase may arise from sample regions with varying elastic properties [30]. Therefore, a phase change is not necessarily correlated with an amplitude change and acts as a disturbance on the amplitude estimation. Consider the signal of the form

$$s(t) = \sum_{i=1}^{3} S_i(t) \sin\left(2\pi f_i t + \phi_i(t)\right) + v \qquad (23)$$

where each frequency component f_i is related to the i-th eigenmode of an AFM cantilever, the respective amplitudes $S_i(t)$ are related to the oscillation amplitudes and v is a white noise process with standard deviation σ. The signal is plotted in Fig. 3(a) and its power spectral density (PSD) is shown in Fig. 3(b). While the inset clearly depicts the multifrequency character of the signal, the amplitude change at the higher frequency components is not obvious. In order to characterize v, the noise density was obtained by integrating the PSD over the frequency range from DC to $2.5\,\mathrm{MHz}$ of a thermal noise measurement taken with the optical beam deflection sensor (not shown) [31] which yields a standard deviation of $\sigma = 1.9\,\mathrm{mV}$. Assuming a Gaussian distribution, the histogram can be plotted in Fig. 3(c). To demonstrate the effect of white noise rejection of the proposed method we used $\sigma = 5\,\mathrm{mV}$ and subsequently set the Kalman filter covariance of the measurement noise to $R = \sigma^2$.

The simulation results are shown in Fig. 4 where each amplitude S_i and each phase ϕ_i experiences a step change of varying magnitude at different points in time. It can be clearly observed how the amplitude and phase changes are accurately tracked for each of the three frequencies. A small transient response is noticeable in the amplitude (phase) estimate if there is a step change in the phase (amplitude). It can be seen that the magnitude of the transient responses in the amplitude estimate due to a phase change are magnified for higher frequency estimates. Here, a tradeoff has to be made between estimation bandwidth and rejecting the coupling between phase and amplitude change. Lowering the Q entries for the higher frequency modes reduces the maximum transient spike due to coupling but comes at the expense of tracking bandwidth.

IV. IMPLEMENTATION

A. Hardware

In order to implement a Kalman filter to reliably estimate amplitude and phase of frequencies up to $1\,\mathrm{MHz}$, high-bandwidth components must be selected. Here, we utilize a Xilinx Kintex-7 KC705 evaluation board (model: XC7K325T) with an internal clock rate of $200\,\mathrm{MHz}$. The FPGA board is interfaced with a DC-coupled high-speed 4DSP input/output (I/O) card (model: FMC151) instrumented with a two channel 14-bit Analog-to-Digital converter (ADC) and a two channel 16-bit Digital-to-Analog converter (DAC) clocked at $250\,\mathrm{MHz}$ and $800\,\mathrm{MHz}$, respectively. For trimodal AFM, ideally an I/O card with eight DACs would be necessary to simultaneously output the cantilever driving signal, three amplitude and three phases of the deflection signal and the estimated DC offset.
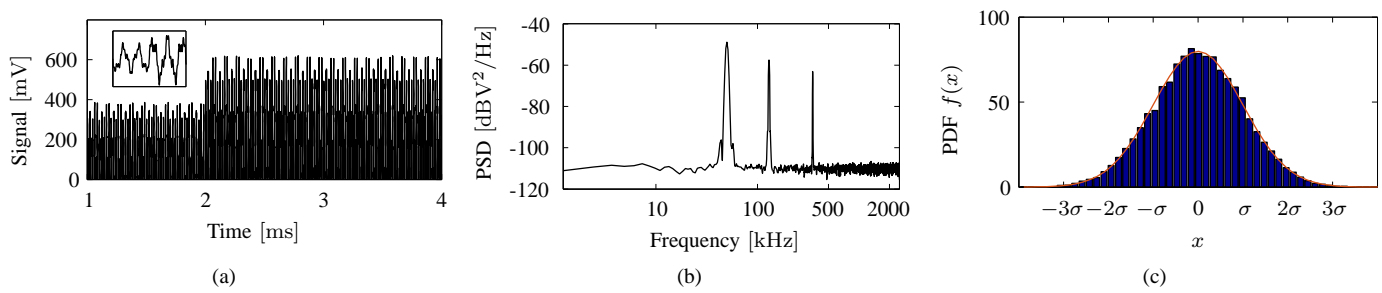
Fig. 3. (a) Simulated multifrequency signal with modulated amplitude, phase and additive white noise v $(-)$ and (b) its power spectral density estimate. (c) Histogram $(-)$ and theoretical probability density function (PDF) $(-)$ of noise process v. Simulation Parameters: $f_{1/2/3} = 50/130/350\,\text{kHz}$, $S_{1/2/3} = 250/100/50\,\text{mV}$, $\sigma = 5\,\text{mV}$, $f_s = 5\,\text{MHz}$.
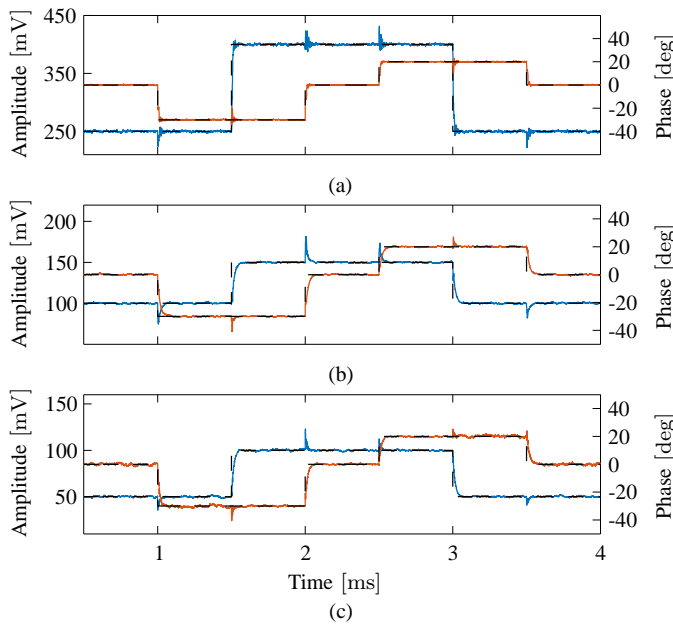

Fig. 4. Amplitude estimate $(-)$, phase estimate $(-)$ and reference $(--)$ of (a) first mode with $Q_1 = 10^{-7}$, (b) second mode with $Q_2 = 10^{-8}$ and (c) third mode with $Q_3 = 10^{-8}$ for amplitude and phase modulated signal and additive white noise with simulation parameters as in Fig. 3.
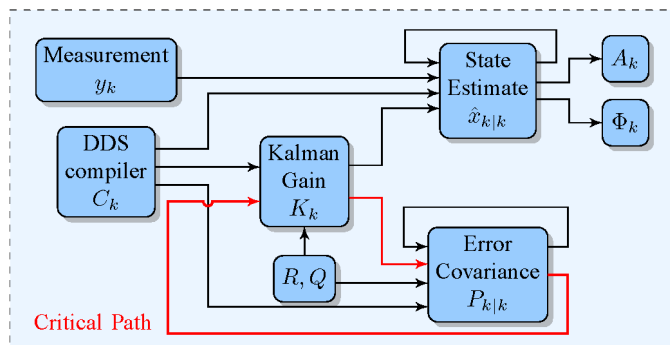

Fig. 5. Block diagram highlighting the main modules of the multifrequency Kalman filter implementation and the critical path.

Due to the limited number of channels, we switch between the signals of interest but the four digital output ports of the evaluation board could be employed using sigma-delta modulation and low-pass filtering.

B. Firmware Design

The digital signal processing system (DSP) design of the proposed multifrequency Kalman filter was split into the design of four sub-modules, i.e. Kalman gain, error covariance, state estimation and amplitude and phase calculation as depicted in Fig. 5. The sinusoidal references are generated with Direct Digital Synthesizer (DDS) compilers. Within the sub-modules, specific Xilinx logic cores are utilized which in turn use dedicated high-speed DSP logic slices implemented in a pipelined structure. The two largest modules, the Kalman gain calculation and the error covariance posterior update, define the critical path and therefore dictate the overall achievable speed of the implementation. Here, the Kalman gain computation

$$K_k = P_{k|k-1} C_k^T \left(C_k P_{k|k-1} C_k^T + R \right)^{-1} \quad (24)$$

is parallelized by computing an intermediate value

$$Z_k = P_{k|k-1} C_k^T \quad (25)$$

and simplified by exploiting the symmetry of P_k. In case of the error covariance update,

$$P_{k|k} = (I - K_k C_k) P_{k|k-1} (I - K_k C_k)^T + K_k R K_k^T, \quad (26)$$

we again make use of the symmetry and only calculate the upper triangular values in order to reduce the complexity and to maintain the positive definite nature of P_k. A matrix multiply module is constructed which pipelines the multiplication of two 7x7 matrices through the use of a state machine and Xilinx logic core multipliers and adders on the lowest level. As the priori state prediction has no dynamics, a simple wire is used to feed back the states at each sample period. The posterior state update is realized using a tree multiply-add architecture with Xilinx logic cores. Note, that this module runs in parallel with the much larger and slower error covariance update module and therefore does not contribute to the critical path. Finally, amplitude and phase are calculated by converting the in-phase and quadrature states into polar form using the CORDIC algorithm [32]. In summary, each module has been designed to balance speed, memory usage and latency. As such, an overall speed of $1.5\,\text{MHz}$ has been achieved for the 7x7 Kalman filter, enabling the state estimation for resonance frequencies up to $750\,\text{kHz}$.
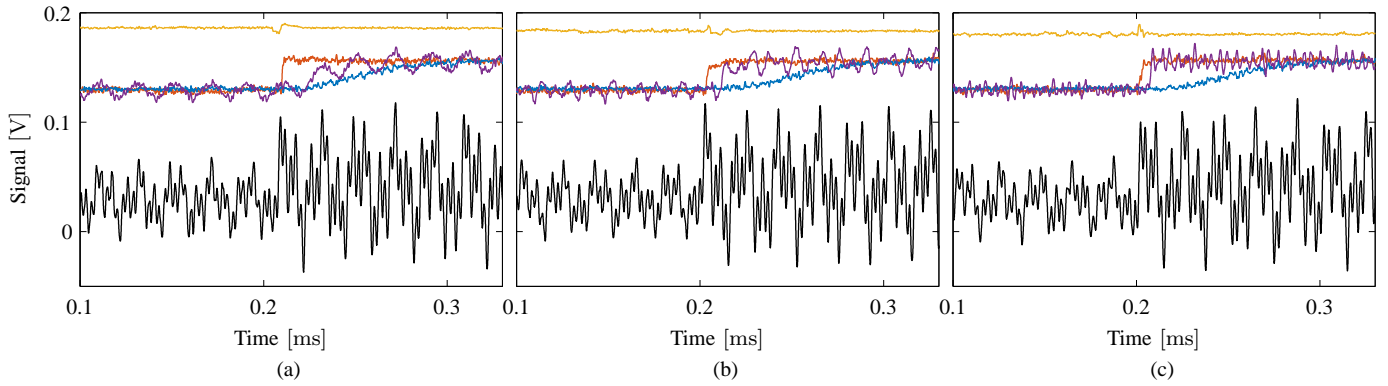
Fig. 6. Amplitude modulated multifrequency signal (—) with slow LIA estimate (—), fast LIA estimate (—), Kalman filter estimate (—) and Kalman filter phase estimate (—) corresponding to a carrier frequency of (a) $f_1 = 50\,\text{kHz}$, (b) $f_2 = 130\,\text{kHz}$ and (c) $f_3 = 350\,\text{kHz}$.

V. EXPERIMENTAL RESULTS

A. Experimental Setup

The performance of the implemented Kalman filter was experimentally assessed and compared with a state-of-the-art lock-in amplifier (Zürich Instruments HF2LI) which provides flexible post-mixing low pass filter settings. Multifrequency amplitude and phase modulated signals corresponding to the first three flexural modes of an AFM cantilever (Bruker DMASP) were either hard coded into the FPGA itself or generated using laboratory function generators (Agilent 33210A). Time-domain data was captured with a digital oscilloscope (Agilent Infiniium DSO90254A) and with the four channel acquisition front-end of a micro system analyzer (Polytec MSA-050-3D).

B. Tracking Bandwidth

We investigate the amplitude tracking bandwidth of the Kalman filter and the LIA for a multifrequency signal of the form

$$s(t) = \sum_{i=1}^{3} S_i(t) \sin\left(2\pi f_i t\right) \quad (27)$$

in time and frequency domain. The frequencies f_i were chosen to approximate the first three resonance frequencies of a tapping-mode cantilever with stepped geometry (compare Section VI) and the driving amplitudes were stepped from $25\,\text{mV}$ to $50\,\text{mV}$.

For each frequency, we compare the Kalman filter at maximum bandwidth with a slow LIA employing a 4th-order LPF with cut-off frequency of $5\,\text{kHz}$ and a fast LIA with cut-off frequencies of $10, 25, 80\,\text{kHz}$, respectively for each modeled frequency. The quality of the estimated amplitude is evaluated based on the tracking bandwidth and noise in the estimate. It can be seen in Fig. 6 how the Kalman filter consistently provides the fastest estimate with the lowest noise compared to both the slow and the fast LIAs. While the noise of the slow LIA is comparable to the Kalman filter amplitude estimate, the fast LIA shows significant 2ω oscillation due to insufficient filtering of the post-mixing frequency components. Also visible is the phase estimate of the Kalman filter which shows the
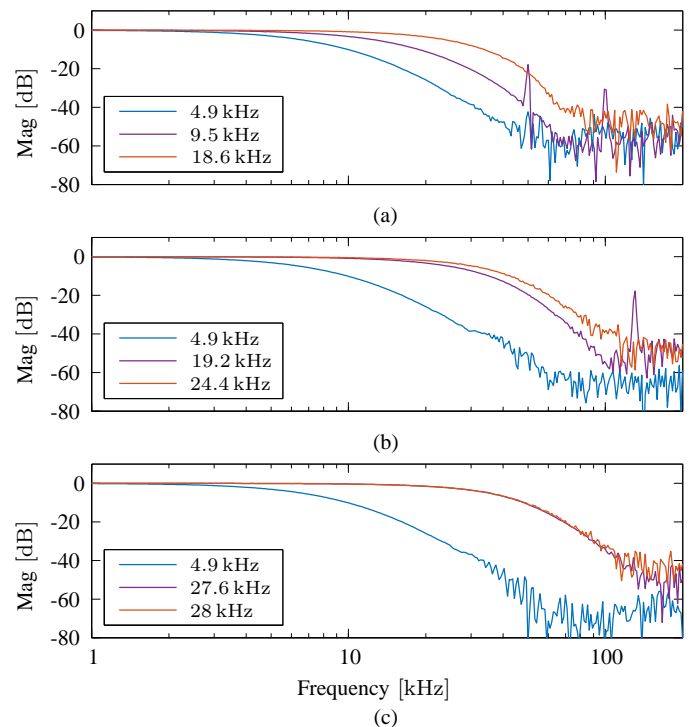

Fig. 7. Frequency response of the slow LIA (—), fast LIA (—) and Kalman filter (—) for an FM-AM experiment for a carrier frequency of (a) 50 kHz, (b) 130 kHz and (c) 350 kHz. The legend shows the $-3\,\text{dB}$ tracking bandwidth. Color coded according to Fig. 6.

characteristic coupling as predicted by the simulations shown in Fig. 4.

The ultimate tracking bandwidth of either amplitude estimation scheme is experimentally verified by performing a frequency sweep of an amplitude modulating signal for each carrier frequency. This FM-AM concept directly reveals the low pass filter characteristic of the Kalman filter and of the post-mixing filters of the LIA and allows for a direct extraction of the $-3\,\text{dB}$ bandwidth. The results are shown in Fig. 7 and carry the same color code as in Fig. 6. It can be seen that for each frequency whose amplitude is to be estimated, the Kalman filter provides the largest bandwidth. Moreover, spikes can be noticed in the frequency response of the fast LIAs at
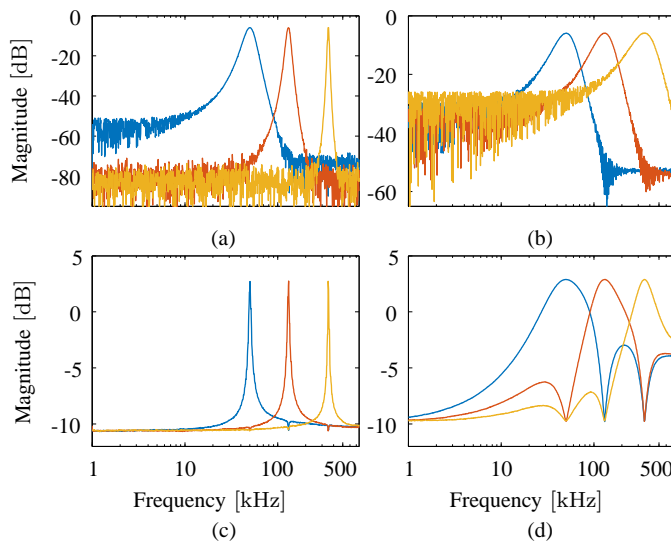
Fig. 8. Frequency response of (a) slow LIA, (b) fast LIA, (c) slow Kalman filter and (d) fast Kalman filter for carrier frequencies of $50\,\text{kHz}$ $(-)$, $130\,\text{kHz}$ $(-)$ and $350\,\text{kHz}$ $(-)$.

ω and 2ω in Fig. 6(a) and Fig. 6(b), i.e. when the carrier frequency is low compared to the bandwidth. The spikes are due to the fact that the LIA recovers both, the carrier frequency itself and the large 2ω component present in the estimate. The results emphasize the fact that the Kalman filter is superior to the LIA when carrier frequencies are small compared to the necessary tracking bandwidth. While the tracking bandwidth of the LIA can be increased by choosing a large low pass filter cut-off frequency, the amplitude estimate becomes increasingly distorted by the 2ω component.

C. Off-Mode Rejection

We analyze the off-mode rejection of the LIA and the Kalman filter by performing a frequency sweep on the signal to be demodulated when specific frequency components are modeled. For comparison, we chose the same frequencies as in previous experiments. The results shown in Fig. 8 indicate the performance of the LIA and the Kalman filter for both, a narrow bandwidth (slow) demodulation and a wide bandwidth (fast) demodulation. It is clear from Fig. 8(a) that the low bandwidth LIA, being a narrowband demodulation device by construction, shows the largest maximum off-mode rejection (measured as the difference between the magnitude at the carrier frequency and at $1\,\text{kHz}$) of around $45\,\text{dB}$ for the first, $67\,\text{dB}$ for the second and $70\,\text{dB}$ for the third carrier frequency.

If the LPF bandwidth is increased, the maximum off-mode rejection drops to around $25\,\text{dB}$ for all frequencies as can be seen in Fig. 8(b). In contrast, the Kalman filter with an equivalent bandwidth of $5\,\text{kHz}$ only achieves a maximum off-mode rejection of $13\,\text{dB}$ for all frequencies shown in Fig. 8(c). For the maximum bandwidth Kalman filter, depicted in Fig. 8(d), the maximum off-mode rejection is $12.5\,\text{dB}$. It can be observed that the off-mode rejection is maximized at frequencies modeled by other Kalman filter states. It can be concluded that by modeling more frequencies, the same off-mode rejection can be achieved as in Fig. 8(c) without sacri-
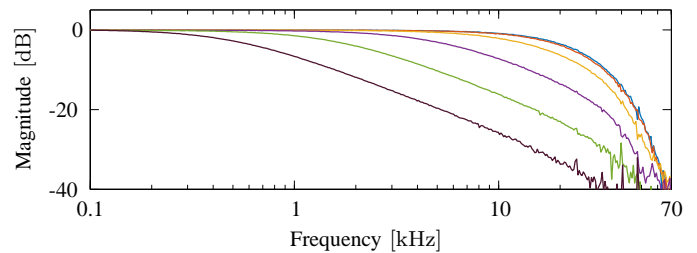

Fig. 9. Magnitude frequency response of the Kalman filter for a fixed carrier frequency of $50\,\text{kHz}$ for different bandwidths by varying the amount of assumed process noise Q.
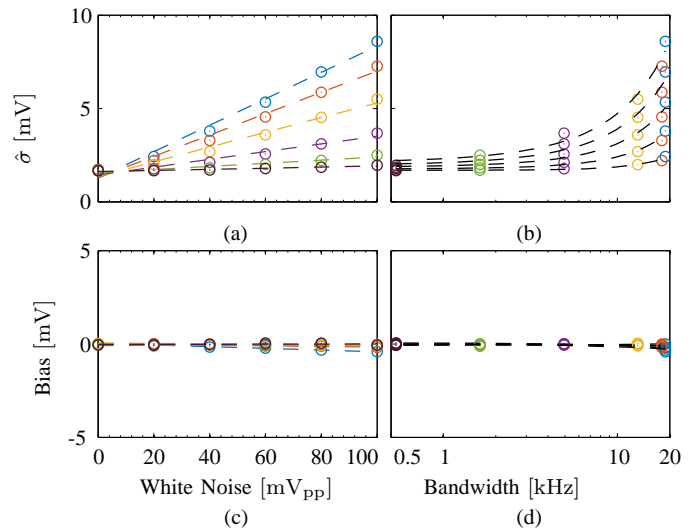

Fig. 10. (a) RMS noise of amplitude estimate from Kalman filter with varying bandwidths according to Fig. 9 as a function of additive white noise and (c) bias of amplitude estimate. (b) RMS noise of amplitude estimate for varying magnitude of additive white noise as a function of Kalman filter bandwidth and (d) bias of amplitude estimate. Color coded according to Fig. 9.

ficing the tracking bandwidth. On the contrary, the maximum LIA off-mode rejection shows a strong dependence on the tracking bandwidth.

D. Noise and Bias Discussion

The maximum obtainable resolution during dynamic mode AFM imaging is dictated by the noise present in the imaging signals. Here, the prominent contributing subsystems are the nanopositioning system, specifically the displacement sensor and high-voltage amplifier [33] and cantilever deflection read-out method [34] in cascade with the demodulator [35]. Since any additional component inevitably adds noise, it is of interest to verify the performance of the Kalman filter to additive sensor induced measurement noise as a function of the tracking bandwidth. The input to the Kalman filter is connected to a function generator with adjustable additive white noise. The estimated amplitude is passed through a high order anti-aliasing LPF with cut-off frequency of $1.2\,\text{MHz}$ and sampled at $f_s = 2.56\,\text{MHz}$ for $T = 13.11\,\text{s}$. The standard deviation (RMS noise) of the estimate $\hat{\sigma}$ is obtained by integrating the noise density estimate from DC to $f_s/2$ using Welch's method without averaging nor overlap. The total integrated noise is used as the performance metric.
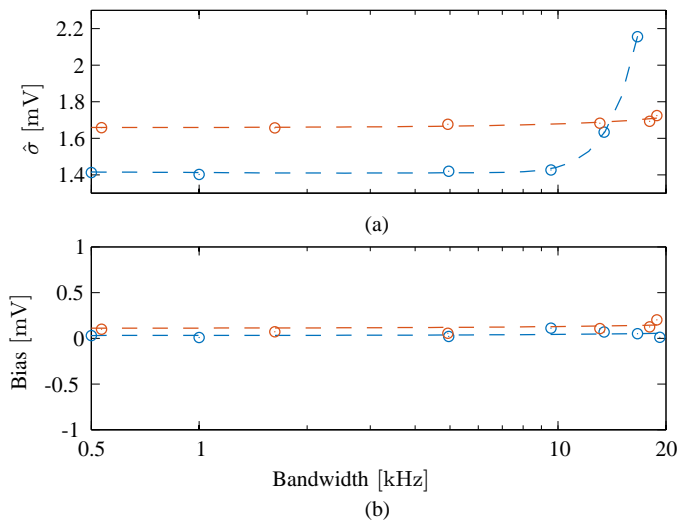
Fig. 11. (a) RMS noise and (b) bias of amplitude estimate from Kalman filter (−) and LIA (−) as a function of tracking bandwidth without additive white noise.

Fig. 12. Multifrequency signal (−) experiencing a step in the offset (−) and offset estimates obtained from a slow LPF (−), fast LPF (−), maximum-bandwidth Kalman filter (−) and reduced-bandwidth Kalman filter (−).

Fig. 13. (a) 2D, (b) 3D topography in and (c) 2D, (d) 3D static deflection in while imaging a PS/LPDE polymer sample in tapping-mode.

The Kalman filter was set to several different tracking bandwidths ranging from 500 Hz to almost 20 kHz as shown in Fig. 9. In Fig. 10(a) it can be seen that a larger tracking bandwidth clearly leads to a larger RMS noise in the amplitude estimate while maintaining a constant bias plotted in Fig. 10(c) (compare color coded Kalman filter frequency responses in Fig. 10(a). A linear fit of the measurement points reveals very good linearity for varying degrees of additive white noise. If the RMS noise of the amplitude estimate is plotted against the Kalman filter bandwidth, a plot such as Fig. 10(b) is obtained. This measurement allows for a direct determination of the resolution for a given imaging bandwidth. The quadratic fit of the measurement points confirms the proportionality of resolution with the square-root of the bandwidth. Fig. 10(d) reveals the unbiased estimate of the Kalman filter as a function of bandwidth.

In the absence of additive white noise, the RMS noise of the amplitude estimate obtained from the Kalman filter is compared with the demodulated amplitude of the LIA as a function of the tracking bandwidth in Fig. 11. The RMS noise of the Kalman filter estimate only increases slightly from 1.66 mV for the smallest bandwidth of 500 Hz to 1.73 mV for the largest bandwidth of 20 kHz. In contrast, the RMS noise of the demodulated amplitude using a LIA, increases quickly when the LPF cut-off frequency is increased above 10 kHz. This is due to the increasing harmonic distortion from frequency components at the carrier and twice the carrier frequency. Above 15 kHz, the Kalman filter shows superior noise performance.

VI. MF-AFM APPLICATION

A. Experimental Setup

The multifrequency Kalman filter was incorporated in an experimental MF-AFM setup as depicted in Fig. 1 using an NT-MDT NTEGRA AFM equipped with a Bruker DMASP piezoele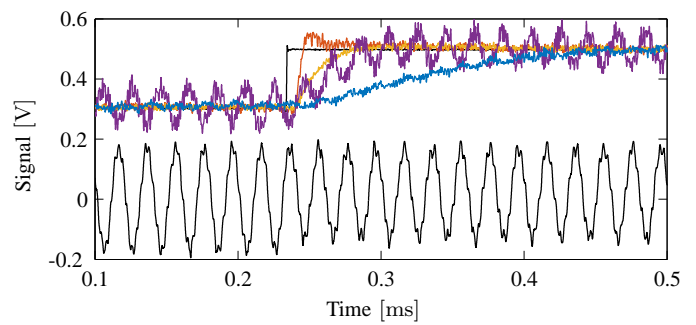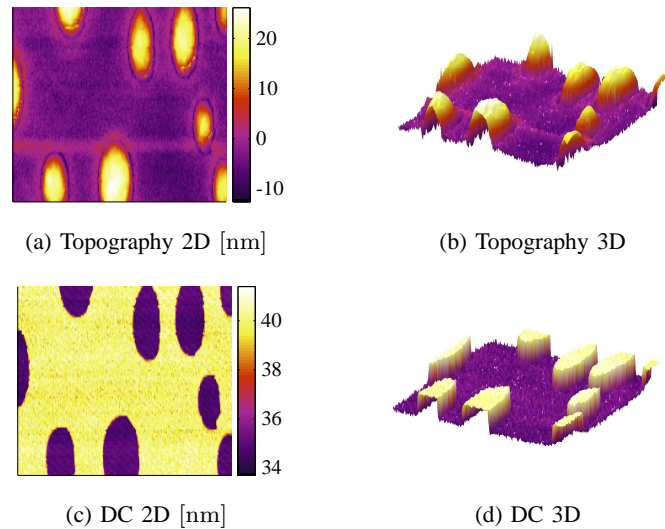ctric cantilever. Due to its stepped geometry, this cantilever has the benefit of having closely spaced eigenmodes [36] benefiting mode-coupling and allowing for the first three flexural modes to be estimated by the Kalman filter. The AFM system was modified to allow for external demodulators providing the feedback signal but is otherwise unaltered. The sample under investigation is a blend of polystyrene (PS) and polyolefin elastomer (ethylene-octene copolymer) (LDPE) available from Bruker (PS-LDPE-12M). The PS regions of the sample have elastic modulus numbers around 2 GPa, while the LDPE regions have elastic modulus numbers around 0.1 GPa, making it a widely used standard to image material contrast. The scan speed was set to 20 μm/s at an area of 10 μm × 10 μm.

B. DC Tracking

The static deflection of the cantilever is usually related to long-range electrostatic and magnetic interaction forces [37] but is generally disregarded in dynamic AFM methods. However, in certain applications such as electric force microscopy or Kelvin force microscopy, novel approaches measure local electric properties of samples at multiple frequencies [38] or use the estimated electrostatic contribution to cancel its
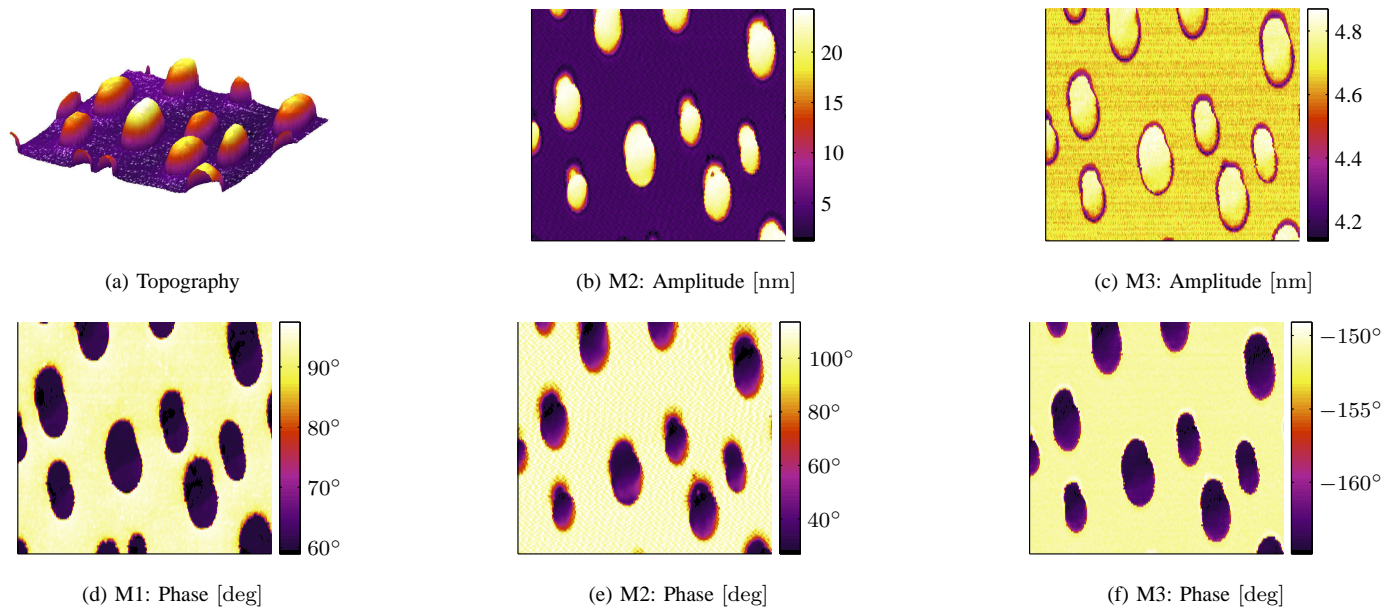
Fig. 14. (a) 3D image of z-axis controller output, 2D image of (b) second mode amplitude, (c) third mode amplitude, (d) first mode phase, (e) second mode phase and (f) third mode phase while imaging a PS/LPDE polymer sample.

effect during a force spectroscopy experiment [39]. Measuring the static deflection of the cantilever during multifrequency excitation can be achieved by using a LIA with zero carrier frequency, directly low-pass filtering the signal or by modeling an additional state in the Kalman filter such as in (12). To demonstrate DC tracking, we excite the piezoelectric cantilever at its first three flexural modes and add a step bias voltage to the driving signal. In response to the bias voltage applied to the piezoelectric layer, the resonances of the cantilever shifts [40] causing a reduction in oscillation amplitude which can be observed in Fig. 12. Further, it can be noticed that the Kalman filter at maximum bandwidth estimates the DC offset with some overshoot which can be accommodated for by reducing the assumed covariance value Q of that respective state. In comparison, a standard 2nd-order LPF with cut-off frequency of $3\,kHz$ cannot achieve the same bandwidth. Increasing the cut-off frequency to $10\,kHz$, yields insufficient suppression of the lowest frequency component present in the signal.

The estimated static deflection of the cantilever can be used as an additional imaging channel during a dynamic AFM experiment as it is not constrained by the z-axis feedback loop. For the polymer sample under investigation, it can be observed in Fig. 13, that the DC image yields better contrast than the controller topography channel, comparable to the increased contrast of the higher eigenmode channels.

C. Trimodal AFM Imaging

The two component polymer was imaged using trimodal AFM, i.e. by actively driving the first, second and third eigenmodes of the piezoelectric cantilever. While the z-axis feedback controller maintains a constant amplitude at the fundamental frequency by commanding the z-actuator, the higher modes are left uncontrolled and can respond freely to sample features. As such, the contrast observed in the higher

eigenmode phases is often used to distinguish between material properties [13]. The experimental results are presented in Fig. 14; a plane correction has been applied to the topography image.

Due to limitations on the number of high-speed DAC channels of the I/O card used and given the fact that one channel had to be used to drive the cantilever, only one more imaging channel was available. As such, the same sample area was imaged multiple times with the available output channel iteratively set to the quantities of interest as shown in Fig. 14. Moreover, we note that the z-axis feedback loop was closed using the amplitude of the fundamental mode obtained from the internal LIA, due to the same channel limitations. However, it was shown in earlier work that the Kalman filter fundamental amplitude estimate can be used as the feedback signal without loss of image quality [24]. From the phase image shown in Fig. 14(d), the imaging condition can be derived as being attractive on the PS matrix and repulsive on the LPDE islands for the fundamental mode. The switch between the different imaging regions is one of the main reasons for the strong material contrast observed in the phase signal. As the higher eigenmodes are driven freely, the amplitude channels also provide some contrast. Specifically the third eigenmode seems to be more sensitive to the borderline region around the LPDE islands, which may be explained by the increased stiffness of that mode.

VII. CONCLUSION

In this work, we have presented a demodulator based on the system theoretical modeling of multiple sinusoids, which is implemented in the form of a Kalman filter. Specifically, the time-variant formulation of the model allows for a high-speed, highly parallelized implementation on a Field Programmable Gate Array without the numerical complications

usually associated with estimators of resonant systems. We show that the implemented Kalman filter is superior in terms of tracking bandwidth over the widely used lock-in amplifier. This is particularly true when the tracking bandwidth is close to the carrier frequency and when lower frequencies limit the maximum low-pass filter bandwidth of the lock-in amplifier. This is of special interest for applications in multifrequency AFM, where the frequency of the fundamental mode will limit the achievable tracking bandwidth when demodulation is performed by a lock-in amplifier. The flexibility and performance of the proposed multifrequency Kalman filter is verified during trimodal AFM imaging of a soft polymer compound, highlighting the well-known increased phase contrast of higher order modes due to material property changes. Additional insight can be gained from the static deflection of the cantilever, a measurement that is usually discarded in conventional dynamic AFM imaging.

ACKNOWLEDGMENT

REFERENCES

[1] G. Binnig, C. F. Quate, and C. Gerber, "Atomic force microscope," *Phys. Rev. Lett.*, vol. 56, pp. 930–933, Mar 1986.

[2] D. Sarid, *Scanning Force Microscopy With Applications to Electric, Magnetic and Atomic Forces*. Oxford University Press, 1994.

[3] Y. Martin, C. Williams, and H. Wickramasinghe, "Atomic force microscope-force mapping and profiling on a sub 100-Å scale," *J. Appl. Phys.*, vol. 61, no. 10, pp. 4723–4729, 1987.

[4] T. Albrecht, P. Grütter, D. Horne, and D. Rugar, "Frequency modulation detection using high-Q cantilevers for enhanced force microscope sensitivity," *J. Appl. Phys.*, vol. 69, no. 2, pp. 668–673, 1991.

[5] Q. Zhong, D. Inniss, K. Kjoller, and V. Elings, "Fractured polymer/silica fiber surface studied by tapping mode atomic force microscopy," *Surf. Sci.*, vol. 290, no. 1-2, pp. L688 – L692, 1993.

[6] T. Ando, "High-speed atomic force microscopy coming of age," *Nanotechnology*, vol. 23, no. 6, p. 062001, 2012.

[7] J. R. Lozano and R. García, "Theory of multifrequency atomic force microscopy," *Phys. Rev. Lett.*, vol. 100, p. 076102, Feb 2008.

[8] R. García and E. T. Herruzo, "The emergence of multifrequency force microscopy," *Nature Nanotechnology*, vol. 7, pp. 217–226, 2012.

[9] A. Raman, S. Trigueros, A. Cartagena, A. P. Z. Stevenson, M. Susilo, E. Nauman, and S. Antoranz Contera, "Mapping nanomechanical properties of live cells using multi-harmonic atomic force microscopy," *Nature Nanotechnology*, vol. 6, no. 12, pp. 809–814, 2011.

[10] S. Jesse, S. V. Kalinin, R. Proksch, A. P. Baddorf, and B. J. Rodriguez, "The band excitation method in scanning probe microscopy for rapid mapping of energy dissipation on the nanoscale," *Nanotechnology*, vol. 18, no. 43, p. 435503, 2007.

[11] A. J. Dick and S. D. Solares, "Utilizing off-resonance and dual-frequency excitation to distinguish attractive and repulsive surface forces in atomic force microscopy," *Journal of Computational and Nonlinear Dynamics*, vol. 6, no. 3, p. 031005, 2011.

[12] T. R. Rodriguez and R. García, "Compositional mapping of surfaces in atomic force microscopy by excitation of the second normal mode of the microcantilever," *Appl. Phys. Lett.*, vol. 84, no. 3, pp. 449–451, 2004.

[13] N. F. Martínez, S. Patil, J. R. Lozano, and R. García, "Enhanced compositional sensitivity in atomic force microscopy by the excitation of the first two flexural modes," *Appl. Phys. Lett.*, vol. 89, no. 15, p. 153115, 2006.

[14] D. Ebeling, B. Eslami, and S. D. J. Solares, "Visualizing the subsurface of soft matter: Simultaneous topographical imaging, depth modulation, and compositional mapping with triple frequency atomic force microscopy," *ACS Nano*, vol. 7, no. 11, pp. 10 387–10 396, 2013.

[15] E. T. Herruzo, A. P. Perrino, and R. Garcia, "Fast nanomechanical spectroscopy of soft matter," *Nature communications*, vol. 5, no. 3126, pp. 1–8, 2014.

[16] A. P. Nievergelt, J. D. Adams, P. D. Odermatt, and G. E. Fantner, "High-frequency multimodal atomic force microscopy," *Beilstein Journal of Nanotechnology*, vol. 5, pp. 2459–2467, 2014.

[17] D. Forchheimer, R. Forchheimer, and D. B. Haviland, "Improving image contrast and material discrimination with nonlinear response in bimodal atomic force microscopy," *Nature communications*, vol. 6, no. 6270, pp. 1–5, 2015.

[18] K. S. Karvinen, M. G. Ruppert, K. Mahata, and S. O. R. Moheimani, "Direct tip-sample force estimation for high-speed dynamic mode atomic force microscopy," *IEEE Trans. Nanotechnol.*, vol. 13, no. 6, pp. 1257–1265, Nov 2014.

[19] T. Ando, T. Uchihashi, and T. Fukuma, "High-speed atomic force microscopy for nano-visualization of dynamic biomolecular processes," *Progress in Surface Science*, vol. 83, no. 7-9, pp. 337–437, 2008.

[20] T. Ando, N. Kodera, E. Takai, D. Maruyama, K. Saito, and A. Toda, "A high-speed atomic force microscope for studying biological macromolecules," *Proceedings of the National Academy of Sciences*, vol. 98, no. 22, pp. 12 468–12 472, 2001.

[21] D. Abramovitch, "Low latency demodulation for atomic force microscopes, part I efficient real-time integration," in *American Control Conference*, June 2011, pp. 2252–2257.

[22] K. S. Karvinen and S. O. R. Moheimani, "A high-bandwidth amplitude estimation technique for dynamic mode atomic force microscopy," *Rev. Sci. Instrum.*, vol. 85, no. 2, p. 023707, 2014.

[23] A. Girgis and T. Hwang, "Optimal estimation of voltage phasors and frequency deviation using linear and non-linear kalman filtering: Theory and limitations," *Power Apparatus and Systems, IEEE Transactions on*, vol. PAS-103, no. 10, pp. 2943–2951, Oct 1984.

[24] M. G. Ruppert, K. S. Karvinen, S. L. Wiggins, and S. O. Reza Moheimani, "A kalman filter for amplitude estimation in high-speed dynamic mode atomic force microscopy," *IEEE Trans. Contr. Syst. Technol.*, vol. 24, no. 1, pp. 276–284, Jan 2016.

[25] Z. Liu, Y. Jeong, and C. H. Menq, "Real-time reconstruction of multimode tip motion of microcantilevers in dynamic atomic force microscopy," *IEEE/ASME Trans. Mechatronics*, vol. 21, no. 2, pp. 825–837, April 2016.

[26] M. G. Ruppert, D. M. Harcombe, and S. O. R. Moheimani, "High-speed state estimation for multifrequency atomic force microscopy," in *American Control Conference*, Boston, MA, USA, July 6-8 2016.

[27] A. K. Cline, C. B. Moler, G. W. Stewart, and J. H. Wilkinson, "An estimate for the condition number of a matrix," *SIAM Journal on Numerical Analysis*, vol. 16, no. 2, pp. pp. 368–375, 1979.

[28] R. G. Brown and P. Y. C. Hwang, *Introduction to Random Signals and Applied Kalman Filtering*. John Wiley & Sons Inc., 1997.

[29] D. Simon, *Optimal State Estimation: Kalman, H-Infinity, And Nonlinear Approaches*. John Wiley & Sons Inc., 2006.

[30] J. Tamayo and R. García, "Effects of elastic and inelastic interactions on phase contrast images in tapping-mode scanning force microscopy," *Appl. Phys. Lett.*, vol. 71, no. 16, pp. 2394–2396, 1997.

[31] M. G. Ruppert and S. O. R. Moheimani, "Multimode Q control in tapping-mode AFM: Enabling imaging on higher flexural eigenmodes," *IEEE Trans. Contr. Syst. Technol.*, vol. 24, no. 3, pp. 1–11, 2016.

[32] J. E. Volder, "The cordic trigonometric computing technique," *Electronic Computers, IRE Transactions on*, vol. EC-8, no. 3, pp. 330–334, Sept 1959.

[33] A. J. Fleming, "Measuring and predicting resolution in nanopositioning systems," *Mechatronics*, vol. 24, no. 6, pp. 605 – 618, 2014, control of High-Precision Motion Systems.

[34] M. Dukic, J. D. Adams, and G. E. Fantner, "Piezoresistive AFM cantilevers surpassing standard optical beam deflection in low noise topography imaging," *Scientific Reports*, vol. 5, no. 16393, pp. 1–11, November 2015.

[35] A. J. Fleming and K. K. Leang, *Design, Modeling and Control of Nanopositioning Systems*, M. J. Grimble and M. A. Johnson, Eds. Springer, 2014.

[36] S. Sadewasser, G. Villanueva, and J. A. Plaza, "Modified atomic force microscopy cantilever design to facilitate access of higher modes of oscillation," *Rev. Sci. Instrum.*, vol. 77, no. 7, pp. –, 2006.

[37] S. Morita, F. J. Giessibl, and R. Wiesendanger, *Noncontact Atomic Force Microscopy*. Springer-Verlag Berlin Heidelberg, 2009.

[38] S. Magonov, J. Alexander, and S. Wu, "Advancing characterization of materials with atomic force microscopy-based electric techniques," in *Scanning Probe Microscopy of Functional Materials*, S. V. Kalinin and A. Gruverman, Eds. Springer New York, 2011, pp. 233–300.

[39] M. Guggisberg, M. Bammerlin, C. Loppacher, O. Pfeiffer, A. Abdurixit, V. Barwich, R. Bennewitz, A. Baratoff, E. Meyer, and H.-J. Güntherodt, "Separation of interactions by noncontact force microscopy," *Phys. Rev. B*, vol. 61, pp. 11 151–11 155, Apr 2000.

[40] R. B. Karabalin, L. G. Villanueva, M. H. Matheny, J. E. Sader, and M. L. Roukes, "Stress-induced variations in the stiffness of micro- and nanocantilever beams," *Phys. Rev. Lett.*, vol. 108, p. 236101, Jun 2012.

S. O. Reza Moheimani (F'11) currently holds the James Von Ehr Distinguished Chair in Science and Technology in the Department of Mechanical Engineering at the University of Texas at Dallas. His current research interests include ultrahigh-precision mechatronic systems, with particular emphasis on dynamics and control at the nanometer scale, including applications of control and estimation in nanopositioning systems for high-speed scanning probe microscopy and nanomanufacturing, modeling and control of microcantilever-based devices, control of microactuators in microelectromechanical systems, and design, modeling and control of micromachined nanopositioners for on-chip scanning probe microscopy.

Dr. Moheimani is a Fellow of IEEE, IFAC and the Institute of Physics, U.K. His research has been recognized with a number of awards, including the IFAC Nathaniel B. Nichols Medal (2014), the IFAC Mechatronic Systems Award (2013), the IEEE Control Systems Technology Award (2009), the IEEE Transactions on Control Systems Technology Outstanding Paper Award (2007) and several best student paper awards in various conferences. He is the Editor-in-Chief of Mechatronics and has served on the editorial boards of a number of journals, including the IEEE TRANSACTIONS ON MECHATRONICS, the IEEE TRANSACTIONS ON CONTROL SYSTEMS TECHNOLOGY, and Control Engineering Practice. He currently chairs the IFAC Technical Committee on Mechatronic Systems, and has chaired several international conferences and workshops.

Michael G. Ruppert (S'14) received the Dipl.-Ing. degree in automation technology in production with a specialization in systems theory and automatic control from the University of Stuttgart, Stuttgart, Germany, in 2013. He is currently pursuing the Ph.D. degree in electrical engineering from The University of Newcastle, Callaghan, NSW, Australia. As a visiting researcher, he is also with the Mechanical Engineering Department at The University of Texas at Dallas, USA.

Mr. Ruppert holds post-graduate research scholarships with The University of Newcastle and CSIRO, Clayton, VIC, Australia. His current research interests include the utilization of system theoretic tools in multifrequency atomic force microscopy, and multimode Q control of microcantilevers. Mr. Ruppert received the Academic Merit Scholarship and the Baden-Württemberg Scholarship.
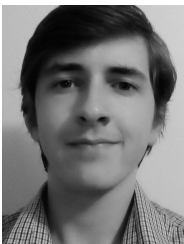
David M. Harcombe is currently completing a Bachelor in Electrical Engineering (Honors) at the University of Newcastle, Newcastle, Australia. His undergraduate studies have led to a focus on control theory, signal processing and digital hardware design.

Mr. Harcombe has been awarded several undergraduate awards including the Faculty of Built Environment Electrical Engineering Scholarships and the Vice Chancellors Honors Scholarship.